Article

Exploring the Photothermo-Catalytic Performance of Brookite TiO$_2$-CeO$_2$ Composites

Marianna Bellardita [1] , **Roberto Fiorenza** [2,*] , **Luisa D'Urso** [2], **Luca Spitaleri** [2,3] , **Antonino Gulino** [2,3], **Giuseppe Compagnini** [2] , **Salvatore Scirè** [2] and **Leonardo Palmisano** [1]

[1] Dipartimento di Ingegneria, Università di Palermo, ed. 6, Viale delle Scienze, 90128 Palermo, Italy; marianna.bellardita@unipa.it (M.B.); leonardo.palmisano@unipa.it (L.P.)

[2] Dipartimento di Scienze Chimiche, Università di Catania, Viale A. Doria 6, 95125 Catania, Italy; ldurso@unict.it (L.D.); lucaspitaleri@hotmail.it (L.S.); agulino@dipchi.unict.it (A.G.); gcompagnini@unict.it (G.C.); sscire@unict.it (S.S.)

[3] I.N.S.T.M. UdR of Catania, Viale A. Doria 6, 95125 Catania, Italy

[*] Correspondence: rfiorenza@unict.it; Tel.: +39-095-738-5012

Abstract: The thermocatalytic, photocatalytic and photothermo-catalytic oxidation of some volatile organic compounds (VOCs), 2-propanol, ethanol and toluene, was investigated over brookite TiO$_2$-CeO$_2$ composites. The multi-catalytic approach based on the synergistic effect between solar photocatalysis and thermocatalysis led to the considerable decrease in the conversion temperatures of the organic compounds. In particular, in the photothermo-catalytic runs, for the most active samples (TiO$_2$-3 wt% CeO$_2$ and TiO$_2$-5 wt% CeO$_2$). the temperature at which 90% of VOC conversion occurred was about 60 °C, 40 °C and 20 °C lower than in the thermocatalytic tests for 2-propanol, ethanol and toluene, respectively. Furthermore. the addition of cerium oxide to brookite TiO$_2$ favored the total oxidation to CO$_2$ already in the photocatalytic tests at room temperature. The presence of small amounts of cerium oxide allowed to obtain efficient brookite-based composites facilitating the space charge separation and increasing the lifetime of the photogenerated holes and electrons as confirmed by the characterization measurements. The possibility to concurrently utilize the photocatalytic properties of brookite and the redox properties of CeO$_2$, both activated in the photothermal tests, is an attractive approach easily applicable to purify air from VOCs.

Keywords: photocatalysis; brookite; cerium oxide; VOCs; air purification

1. Introduction

Nowadays, high quality clean air for both indoor and outdoor environments is strongly recommended. Recently, new and green approaches such as the photocatalytic oxidation of volatile organic compounds (VOCs,), can be considered suitable solutions for an environmental friendly air purification [1]. Compared to more consolidated processes, such as catalytic combustion or physical adsorption. the possibility of an efficient use of sunlight under mild conditions leads to consider photocatalytic applications as an optimal alternative for the removal of dangerous pollutants (VOCs) from the air of our living spaces.

In the last decade, titanium dioxide (TiO$_2$, *titania*)-based photocatalysis has played an important role, TiO$_2$ being an active component of paints, cements, building materials and self-cleaning products [2–6]. The lack of toxicity. the relatively low cost and the good performance especially under UV light irradiation, makes this material one of the most used and studied photocatalysts [7–11]. Recently. the interest in the least common crystalline structure of TiO$_2$, i.e., brookite, increased exponentially, and its superior performance compared to rutile and anatase TiO$_2$ has been reported in several

photocatalytic reactions [12,13]. However, as the other TiO_2 crystalline forms. the wide band-gap (around 3.2–3.4 eV [12]) limits its utilization to only UV irradiation, with a very poor exploitation of the solar light ($\approx$5%). One of the most investigated and performed strategies to shift the absorption properties of TiO_2 towards the visible light is the synthesis of mixed oxides (i.e., composites) [14–16]. In particular. the combination of TiO_2 with CeO_2 (*ceria*) allows to sensibly increase the TiO_2 efficiency in the solar/visible light irradiation range [17,18]. Cerium oxide has interesting properties such as the possibility of favoring the transfer of electrons in its empty 4f energy levels (which facilitates the separation of the charge carriers). the lower band gap (2.7–2.9 eV) compared to TiO_2 (that allows the activation by solar light irradiation). the redox properties that can promote a remarkable mobility of the surface oxygen with a beneficial effect for the oxidation reactions and the formation of Ce^{4+}/Ce^{3+} species [19,20].

In this context, despite the fact that anatase, rutile or mixed anatase/rutile TiO_2 with ceria have been sufficiently studied [21–23]. the photocatalytic, thermocatalytic and photothermo-catalytic performance of pure brookite/CeO_2 systems have not yet been analyzed to the best of our knowledge.

Moreover, although the photocatalytic oxidation is a green and sustainable method to remove low concentrations of VOCs. the reported removal efficiencies are still far from a practical application on an industrial scale [24–26]. The combination of photocatalysis, employing sunlight as the irradiation source, with thermocatalysis, can be considered an optimal compromise to obtain high conversion values that are typical of thermocatalysis, simultaneously decreasing the temperature of the treatments, and favoring a more sustainable energy consumption [23,27].

For this purpose, in this work we compared the catalytic (photo)performance of some mixed brookite TiO_2-CeO_2 composites, for the oxidation in the gas phase of some model VOCs (2-propanol, ethanol and toluene). In particular, we correlated the performance of the catalysts in the thermocatalytic, photocatalytic and photothermo-catalytic oxidation tests to the chemical and structural modifications induced by the ceria addition on pure brookite.

The exploitation of the double synergy (between thermocatalysis and photocatalysis and between the photocatalytic properties of the brookite TiO_2 and the redox properties of CeO_2), can allow to develop a multi-catalytic green and efficient technology for the abatement of VOCs from the air.

2. Results and Discussion

### 2.1. Brookite TiO₂-CeO₂ Composites Characterization

As reported in the literature. the obtainment of pure brookite phase was difficult, being strongly affected by the preparation method adopted [12]. One of the easy and consolidated approaches to prepare pure brookite is the thermohydrolysis of $TiCl_4$ in aqueous chloride solutions [28,29]. With this procedure, it is possible to obtain the brookite phase without the presence of anatase or rutile.

The confirmation of the presence of the only brookite phase was obtained with Raman spectroscopy (Figure 1a). Indeed, this characterization technique is more sensitive to detect the presence of the brookite phase than the XRD one, that required a structure refinement method to clearly note that brookite is the only crystalline structure present [12,30,31]. To investigate the change in the physico-chemical properties of brookite due to the addition of cerium oxide, three different composites were prepared with a growing amount of the hosted CeO_2 oxide (1 wt%, 3 wt% and 5 wt%).

In previous works with anatase and P25 TiO_2, we noted that a CeO_2 concentration higher than 5 wt% had a detrimental effect for the titania photoactivity [23,32]. Consequently, in this work, although we studied another type of TiO_2 sample, we limited our investigations to the low amounts of cerium oxide. The composites were coded as Ti/CeX where X is the weight percentage of CeO_2. This is just a code that does not identify the catalytic support which in this case could be considered to be TiO_2.

From the Raman spectra (Figure 1a) it is possible to note that bare brookite showed, in accordance with the literature [29,33], 13 peaks: six A_{1g}: four clearly visible (153, 246, 414 and 636 cm^{-1}) whereas the other two bands related to this Raman optical mode were at 128 cm^{-1} (as a shoulder of the main

peak at 153 cm^{-1} also visible in Figure 1b) and at about 195 cm^{-1} (with a very low intensity overlapping with the signal at 212 cm^{-1} (B$_{1g}$ mode)). The other Raman vibration modes were two B$_{1g}$ (212 and 325 cm^{-1}), three B$_{2g}$ (365, 462 and 586 cm^{-1}, this latter present with a very low intensity) and two B$_{3g}$ (502 and 545 cm^{-1}). The typical signal at 153 cm^{-1} is a fingerprint of the presence of brookite and the lack of the usual Raman bands at 516 and 448 cm^{-1}, typical of the anatase and rutile phases, respectively [34], which indicates that brookite is the only phase present. Bare CeO$_2$ showed a single band at 462 cm^{-1} related to the cubic fluorite structure (F$_{2g}$ vibration) [20]. All of the TiO$_2$-CeO$_2$ composites exhibited the bands of pure brookite, whereas the signal of CeO$_2$ at 462 cm^{-1} overlapped with the second B$_{2g}$ band of brookite, although it is possible to note a broadening of this band in the mixed oxide samples. A further indication of the composites formation was the slight blue shift of the main brookite Raman band (Figure 1b), more evidently increasing the amount of ceria. The broadening and the shift of the Raman band is, in fact, correlated to the modification of the principal oxide lattice (in this case brookite TiO$_2$) caused by the progressive interaction with the second oxide (in this case CeO$_2$) [35].
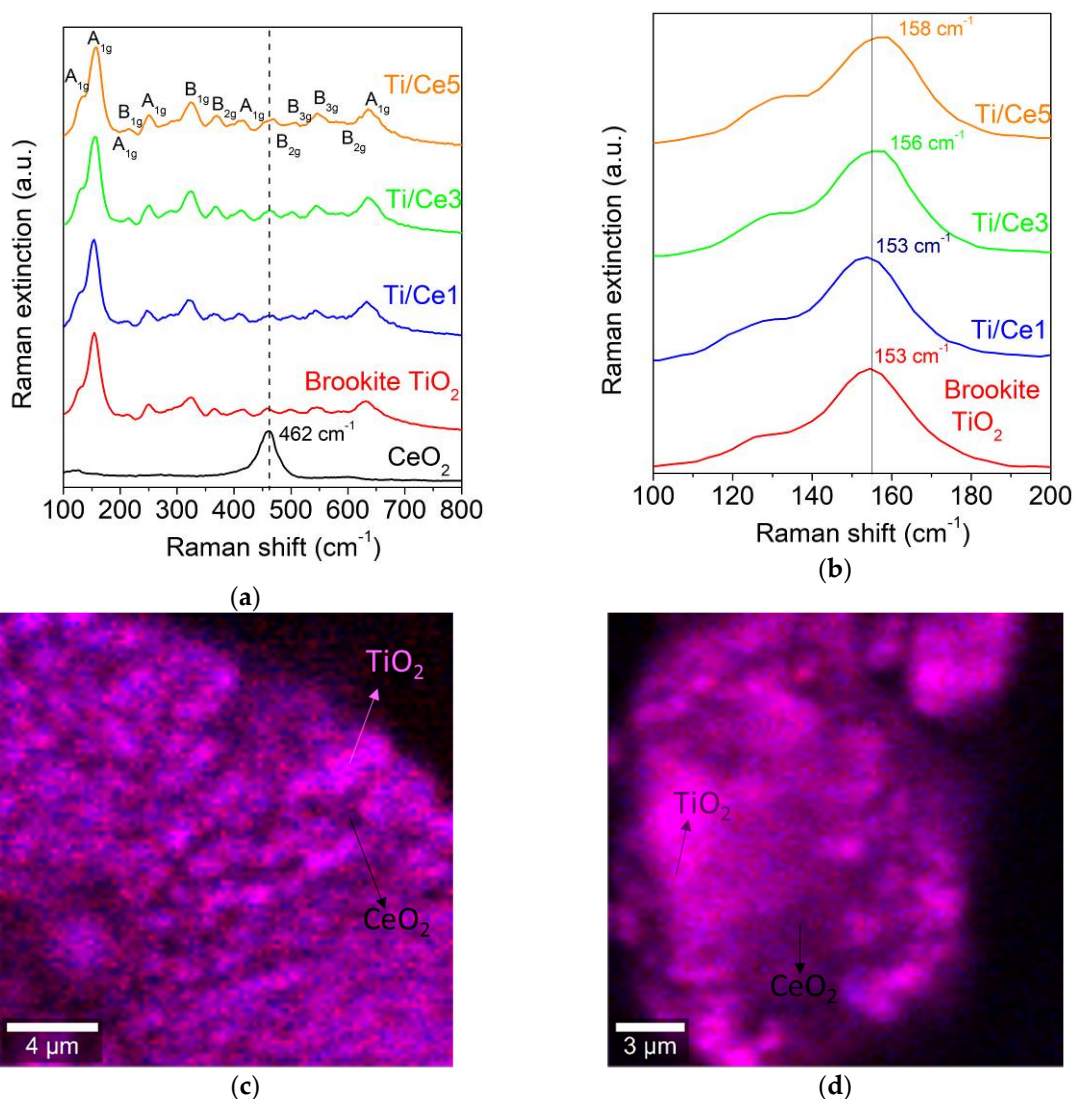
**Figure 1.** (**a**) Raman spectra of the analyzed samples; (**b**) Raman shift of the main brookite band; (**c**) Raman confocal map of the Ti/Ce3 sample; and (**d**) Raman confocal map of the Ti/Ce5 sample.

From the Raman confocal maps (Figure 1c,d illustrating the Ti/Ce3 and the Ti/Ce5 as representative samples), it is possible to note that there are no isolated regions with a prevalence of one color (the clear

violet color area represents the presence of brookite whereas the darker violet area represents the presence of CeO_2, however, which are difficult to differentiate), thus indicating as the low amount of cerium oxide is uniformly present on the brookite [10,18].

The good interaction of the cerium oxide with brookite TiO_2 was also confirmed by the formation of a heterojunction between the two oxides, detectable in the Ti/Ce5 sample through the HRTEM (High Resolution Transmission Electron Microscopy) image (Figure 2), whereas in the other two composites, due to the low amount of the cerium oxide, it was not possible to discern the interface between the titania and ceria, in any case difficult to differentiate, even in the Ti/Ce5 sample, due to the similar d-space values of the examined oxides. However, from Figure 2 it is possible to note the boundary interaction between the brookite TiO_2 (121) planes and the CeO_2 (111) planes accordingly to the d-spacing values [33,36]. The interplanar distance of 0.35 nm referred to the (210) or (111) planes of brookite TiO_2 [37] was not detected in our samples utilizing the employed TEM.
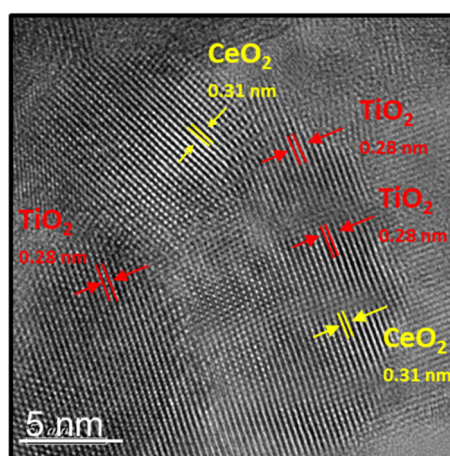
Figure 2. HRTEM (High Resolution Transmission Electron Microscopy) image of the brookite Ti/Ce5 sample.

The specific surface area. the mean pores diameter and the pores volume of the brookite TiO_2-CeO_2 composites are reported in Table 1. Figure 3 displays the nitrogen physisorption curves (Figure 3a) and the distribution of the pores size obtained by the Barrett, Joyner and Halenda (BJH) method (Figure 3b). All the powders showed the characteristic mesoporous type IV isotherm (Figure 3a) [38] and a H1 hysteresis. The addition of cerium oxide diminished the specific surface area (Table 1) calculated with the BET (Brunauer-Emmett-Teller) method, of brookite, reasonably due to the progressive interaction of the hosted oxide with brookite, as confirmed by the Raman measurements, and to the calcination treatment necessary for the formation of the composites.

Interestingly. the bare brookite showed a broader BJH pore size distribution curve (Figure 3b), whereas the pure CeO_2 exhibited the lowest surface area (60 m^2/g) and pore volume (0.14 cm^3/g) with the highest mean pore diameter (32 nm) (Table 1).

Table 1. Brunauer-Emmett-Teller specific surface area (S_A), mean pore diameter (d_p), pore volume (v_p) and optical band-gap (E_g) of the analyzed samples.

Samples	S_A (m^2/g)	d_p (nm)	v_p (cm^3/g)	E_g (eV)
CeO_2	60	32.1	0.14	2.87
Brookite TiO_2	100	27.3	0.33	3.22
Ti/Ce1	69	24.9	0.35	3.20
Ti/Ce3	68	25.2	0.34	3.21
Ti/Ce5	66	24.7	0.33	3.19
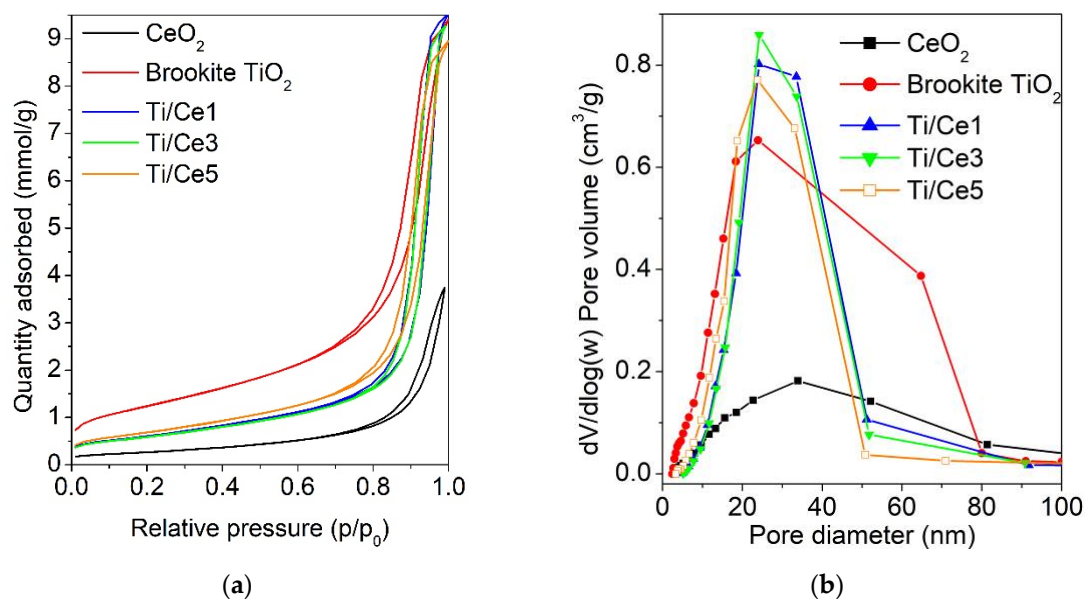
Figure 3. (**a**) Nitrogen physisorption curves and (**b**) the Barrett, Joyner and Halenda (BJH) curves of the analyzed samples.

The diffuse reflectance spectra (DRS) of the materials are shown in Figure 4 (Figure 4a. the Kubelka-Munk function, i.e.. the reflectance function, was plotted versus the wavelength; whereas Figure 4b illustrates the estimation of their optical band-gap through the modified Kubelka-Munk function). It is possible to note (see also Table 1) that the addition of cerium oxide resulted in a slight decrease of the optical band-gap of pure brookite, whereas. the bare CeO_2 showed the highest red shift (Figure 4a) and consequently a lower band-gap (Figure 4b) compared to TiO_2, in accordance with the literature data [17,32].
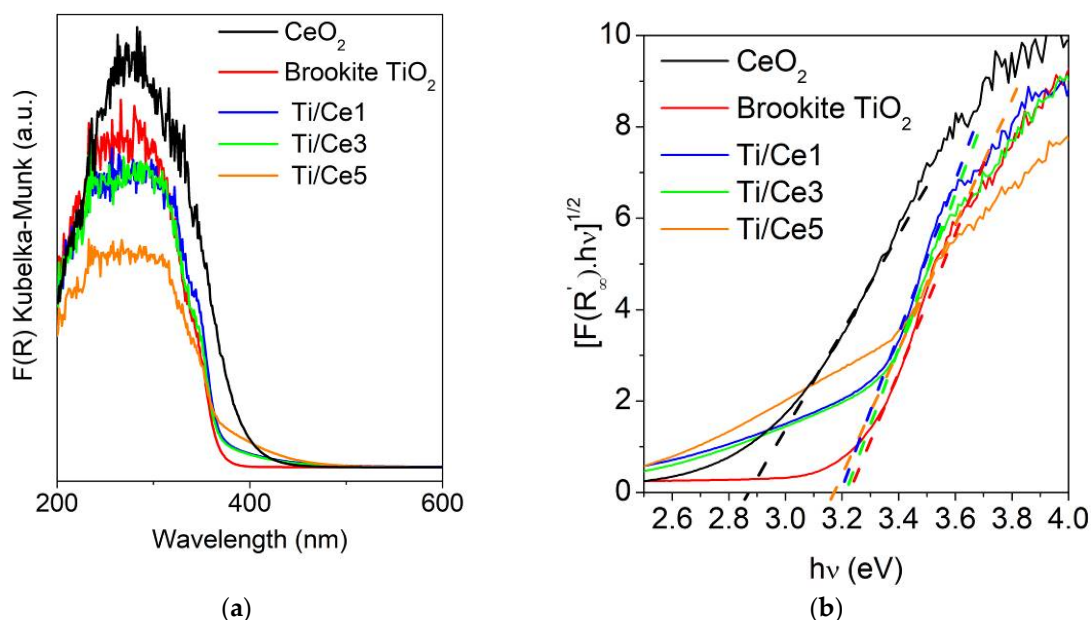
Figure 4. (**a**) Kubelka-Munk function (reflectance function) versus the wavelength and (**b**) the modified Kubelka-Munk function versus the hν for the investigated samples.

Figure 5 reports the photoluminescence (PL) spectra of the investigated samples. The band at 388 nm, assigned to the band-to-band emission of brookite TiO_2 [39–41], was progressively quenched

increasing the amount of cerium oxide on TiO_2, pointing to a lower recombination rate between the photoholes and photoelectrons in the TiO_2-CeO_2 composites. Indeed. the decrease of the PL band intensity is usually related to an enhancement of the charge carrier separation in the photoactive materials [42,43]. In the TiO_2-CeO_2 composites, also the intensity of the PL brookite band at about 430 nm, due to the self-trapped excitons confined in the TiO_6 octahedra [44], decreased, whereas the PL band at 460 nm of pure brookite, attributed to the presence of oxygen vacancies in the TiO_2 lattice [44,45], overlapped with the band at 455 nm due to the band-to-band emission of CeO_2 [10,32]. Even for these bands. the intensity diminution in the composites was a further indication of the better separation of the charge carriers in the Ti/Ce powders. Finally. the PL band at about 555 nm, present in all of the samples, was related to the photoelectrons trapped in the defect centers generated by the oxygen vacancies of titania and/or ceria [46].
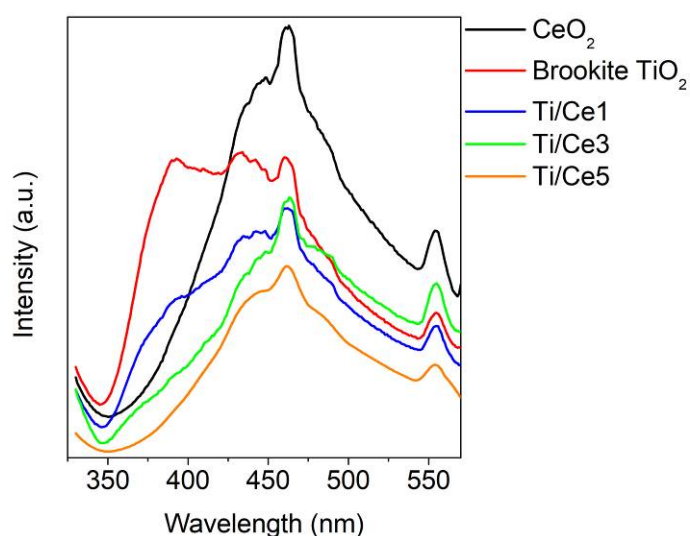

Figure 5. Photoluminescence spectra of the analyzed samples ($\lambda_{excitation}$ = 300 nm).

2.2. Surface Properties of Brookite TiO_2-CeO_2 Composites

The X-ray photoelectron spectroscopy (XPS) results of pure brookite TiO_2 confirmed the presence of only this crystalline form of TiO_2. Indeed. the sharp Ti $2p_{3/2,1/2}$ spin–orbit components at 459.3 and 465.1 eV (5.8 eV spin–orbit coupling, Figure S1a) and the O 1s band centered at 530.8 eV (Figure S1b), are typical of brookite phase [47,48]. It has been noted that the absence of broadening at low binding energy (BE) due to a doublet in the titania band (ascribed to Ti^{3+}) [49]. The O 1s spectral profile suggests the presence of some Ti–OH hydroxide species, evident at a higher binding energy with respect to the main peak.

As regards the XPS ionization of the 3d cerium levels of the cerium oxide sample, six distinct signals were obtained (Figure S1c), in accordance with the literature data for the pure CeO_2 species [50,51]. The ground state for Ce^{4+} is represented by the $3d^{10}4f^0$ electronic configuration. In this context. the bands at 882.9, 889.2 and 898.8 eV are ascribed to the Ce $3d_{5/2}$ states, whereas the peaks at 901.5, 907.8 and 917.3 were assigned to the Ce $3d_{3/2}$ states (18.6 spin–orbit coupling). In accordance to the literature data [50–52]. the signals at 882.9 and 889.2 eV were due to a mixed configuration of $3d^94f^2$(O $2p^4$) and $3d^94f^1$(O $2p^5$) Ce^{4+} states, while the signal at 898.8 eV corresponds to the $3d^94f^0$(O $2p^6$) Ce^{4+} state. Finally. the peaks at 901.5, 907.8 and 917.3 were consistent with the spin–orbit components of the $3d_{3/2}$ states of the same configurations. Therefore, only the peaks expected for pure CeO_2 were observed. Furthermore. the absence of signals at 882.9, 889.2 and 898.8 eV excludes any $3d^94f^1$ (O $2p^6$) and $3d^94f^2$(O $2p^5$) Ce^{3+} final states. Figure S1d shows the high-resolution O 1s band for the pure cerium oxide that involves two signals at 529.4 and 531.6 eV, respectively. The first peak is due to the O^{2-} species for CeO_2, whereas the latter is assigned to the OH^- species [52].

The spectrum of the Ti/Ce5 sample displays the Ti 2p 3/2 and 1/2 spin–orbit peaks at 459.0 and 464.8 eV (Figure 6a) [48,53]. Therefore, these Ti 2p levels were just 0.3 eV at lower binding energies compared to the bare brookite catalyst and can be rationalized in terms of the higher electronegativity of Ti (1.5) with respect to that of Ce (1.1). This sizeable shift suggests some electronic interaction between titanium and cerium cations. Moreover, these XPS binding energies are the same also considering the Ti/Ce1 and the Ti/Ce3 catalysts (Table 2).
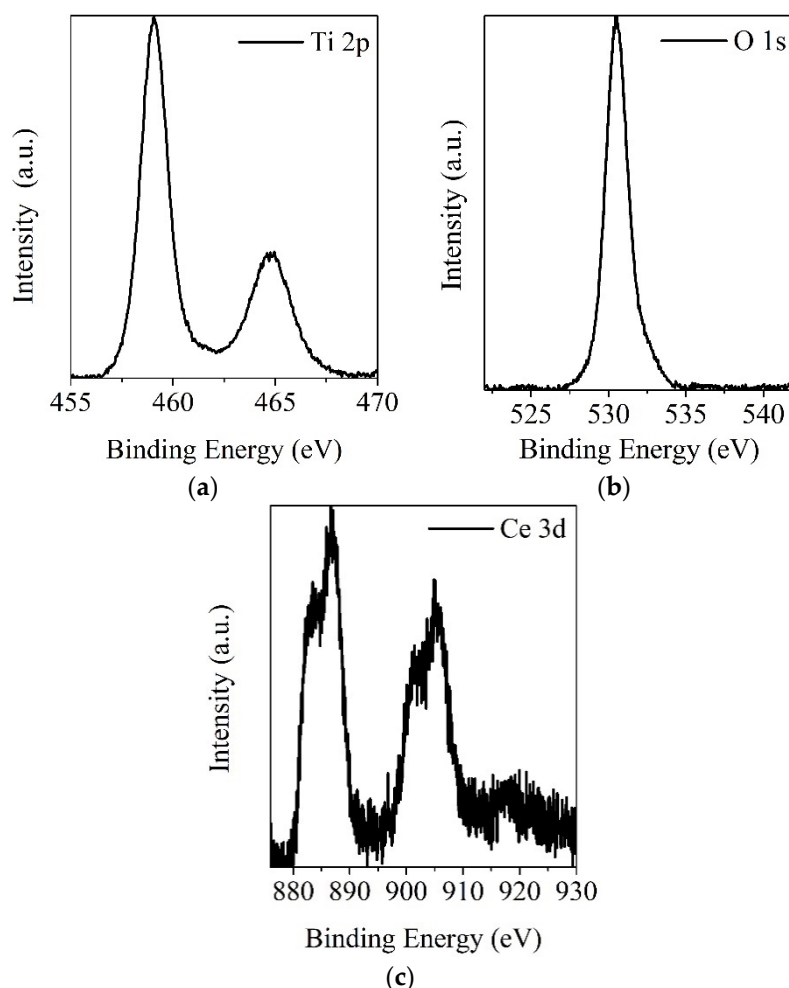
Figure 6. (**a**) Al Kα-excited XPS of the Ti/Ce5 composite obtained in the Ti 2p zone; (**b**) in the O 1s binding energy region and (**c**) in the Ce 3d binding energy region. Structure due to the satellite radiation was subtracted from the spectra.

Table 2. Binding energies (eV) obtained by XPS for the analyzed materials.

Samples	O 1s	Ti 2p$_{3/2,1/2}$	Ce 3d$_{5/2,3/2}$
CeO$_2$	529.4, 531.6	/	882.9–901.5, 889.2–907.8, 898.8–917.3
Brookite TiO$_2$	530.8	459.3–465.1	/
Ti/Ce1	530.5	459.0–464.8	883.2–901.8, 886.5–905.1, 917.5
Ti/Ce3	530.5	459.0–464.8	883.2–901.8, 886.5–905.1, 917.5
Ti/Ce5	530.5	459.0–464.8	883.2–901.8, 886.5–905.1, 917.5

The high-resolution spectrum of the O 1s core level for the Ti/Ce5 sample (Figure 6b), and those for both Ti/Ce1 and Ti/Ce3 analogues (Table 2), show a sharp O 1s peak at 530.5 eV, similar to the bare brookite [47,48]. Moreover, this peak suffers a 0.3 eV lower binding energy shift, compared to the un-modified titania.

The Ce 3d binding energy region of Ti/Ce5 (Figure 6c) shows the typical superimposition of Ce^{4+} and Ce^{3+} contributions [48,51,53]. The lower binding energy doublet at 883.2 and 901.8 eV (18.6 eV spin-orbit coupling) is attributed to the state of Ce(IV) $3d^9 4f^2 (O\ 2p^4)$ [48,51], while the doublet at 886.5 and 905.1 eV (18.6 eV spin-orbit coupling) is attributed to the state of Ce(III) $3d^9 4f^2 (O\ 2p^5)$ [50,53]. Moreover. the presence of Ce^{4+} is confirmed by the characteristic low peak at 917.5 eV [48,51]. All these observations are in agreement with those previously reported for the XPS of Ce^{4+} and Ce^{3+} mixed valence state systems [32,50,53].

For similar systems, it was reported that the presence of Ce^{3+} species may be attributed to electronic interactions between TiO_2 and CeO_2 that cause the partial reduction of the Ce tetravalent cation [32,53]. Obviously. the presence of some Ti^{3+} cations on the TiO_2 surface must be considered why this redox process takes place. Even though we have no XPS evidence of such Ti species, it is widely recognized that the not complete axial coordination of the surface Ti cation in TiO_2 leads to some surface Ti reduction [54,55]. Reasonably, any chemical interaction between the two oxides should be confined to the topmost ionic layers of each oxide nanoparticles, and this is consistent with the formation of a heterojunction between the titania and ceria interfaces as confirmed by the HRTEM (Figure 2).

On the basis of the above observation, we noted that the Ti 2p levels of the mixed oxides are shifted at a 0.3 eV lower BE compared to bare brookite, while the binding energy of the Ce^{4+} 3d levels in the TiO_2-CeO_2 mixed oxides are 0.3 eV at higher BE in comparison to the same signal detected in CeO_2 (882.9 eV). This confirms the existence of an electronic interaction between the Ti and Ce (both Ce^{3+} and Ce^{4+}) ions [32,48].

Interestingly, as also already reported in the literature [47]. the increase of the amount of ceria in the composites parallelly decreases the intensity of the XPS peaks of Ce^{4+} whilst it enhances those of Ce^{3+}. The XPS Ce(III)/Ce(IV) atomic ratio was investigated using a method already reported [53]. This method considers the relative intensities of the Ce(III) and Ce(IV) XPS 3d bands, obtained by the fitting of the experimental spectrum. We are aware that all the final states of the ionizations of the Ce (IV), already discussed for the blank CeO_2 sample (Figure S1c, vide supra), must be included in the band fitting. Moreover. the low intensity high binding energy band (Figure 6c) at 917.5 eV is with no doubt due to the ionic $3d^9 4f^0 (O\ 2p^6)\ 3d_{3/2}\ Ce^{4+}$ state. By taking all these considerations into account, from the XPS spectral fitting of the Ti/Ce5 sample (Figure S1e) we obtained a Ce(III)/Ce(IV) = 1.4 value that stresses a Ce(III) prevalence on the sample surface [56,57]. Finally. the surface composition of the five analyzed powders, was calculated. Results indicate that the Ce/Ti ratios are 0.007, 0.010 and 0.030 for the Ti/Ce1, Ti/Ce3 and Ti/Ce5 systems. These ratios are consistent to the nominal molar ratio of the investigated materials.

2.3. (Photo)Catalytic Oxidation of 2-Propanol

The results of the thermocatalytic oxidation in the gas phase of 2-propanol are reported in the Table 3, where the T_{10}, T_{50} and T_{90} are the temperatures at which the 10%, 50% and 90% of conversion is achieved (the relative conversion curves for all the analyzed samples are reported in the supporting information, Figure S2). Interestingly. the high surface area of bare brookite TiO_2 (100 m^2/g, Table 1) allowed to obtain a T_{90} of 258 °C in the alcohol conversion and of 323 °C in the conversion to CO_2, which are 22 °C and 65 °C lower compared to the T_{90} of P25 TiO_2 (80% anatase-20% rutile) under the same experimental conditions [23]. Although the addition of CeO_2 decreased the surface area of brookite (Table 1) the synergism between the two oxides permitted to decrease the 2-propanol conversion temperature that was the lowest for the Ti/Ce3 sample with a T_{90} of 253 °C.

The catalytic combustion of 2-propanol can follow two pathways that led to obtain as intermediate products propene and water or acetone and water [23,58]. In our experimental conditions, acetone was the main detected reaction intermediate, whereas the amount of propene was negligible. Interestingly. the addition of cerium oxide on brookite favored the total oxidation to CO_2. Indeed. the maximum of acetone conversion decreased by increasing the amount of ceria in the brookite. This maximum

varies from 93% (at 261 °C) for pure brookite to 41% for Ti/Ce5, similar to bare CeO_2 (39%), but was achieved at a much lower temperature (221 °C instead of 365 °C). Contextually. the T_{10}, T_{50} and T_{90} values related to the conversion to CO_2 over the composites were lower than those of the bare brookite (Table 3) with the Ti/Ce5 that exhibited the lowest T_{90} (281 °C).

Table 3. The thermocatalytic oxidation of 2-propanol over the investigated samples.

Samples	2-Propanol Conversion	Conversion to CO_2	Maximum Conversion to Acetone
CeO_2	T_{10} = 293 °C T_{50} = 342 °C T_{90} = 417 °C	T_{10} = 336 °C T_{50} = 386 °C T_{90} = 434 °C	39% (365 °C)
Brookite TiO_2	T_{10} = 209 °C T_{50} = 226 °C T_{90} = 258 °C	T_{10} = 271 °C T_{50} = 294 °C T_{90} = 323 °C	93% (261 °C)
Ti/Ce1	T_{10} = 195 °C T_{50} = 222 °C T_{90} = 256 °C	T_{10} = 253 °C T_{50} = 277 °C T_{90} = 306 °C	79% (248 °C)
Ti/Ce3	T_{10} = 194 °C T_{50} = 213 °C T_{90} = 253 °C	T_{10} = 212 °C T_{50} = 260 °C T_{90} = 294 °C	47% (248 °C)
Ti/Ce5	T_{10} = 176 °C T_{50} = 208 °C T_{90} = 257 °C	T_{10} = 199 °C T_{50} = 238 °C T_{90} = 281 °C	41% (221 °C)

The results of the photocatalytic oxidation of 2-propanol after 2 h of simulated solar irradiation at room temperature are reported in the Figure 7. In this case. the brookite TiO_2-CeO_2 composites showed a similar 2-propanol conversion to bare brookite with only a slight increase in the conversion values with the increase of the amount of cerium oxide. The alcohol conversion varies from 60% of pure brookite to 62% of Ti/Ce1 and 66% of Ti/Ce3 and Ti/Ce5. In addition, also in this case acetone was the main intermediate produced, in accordance with the literature data [59,60]. The bare CeO_2 showed the lowest photocatalytic activity with the 22% of 2-propanol conversion, but with the highest selectivity to CO_2 (36%). The presence of ceria allowed to increase the selectivity to CO_2 with respect to the bare brookite (from the 3% of bare brookite to 21% of the Ti/Ce5 sample). This is another indication of a mutual synergism between titania and ceria, while pure brookite was an optimal photocatalyst for the partial oxidation to acetone (selectivity of 95%).
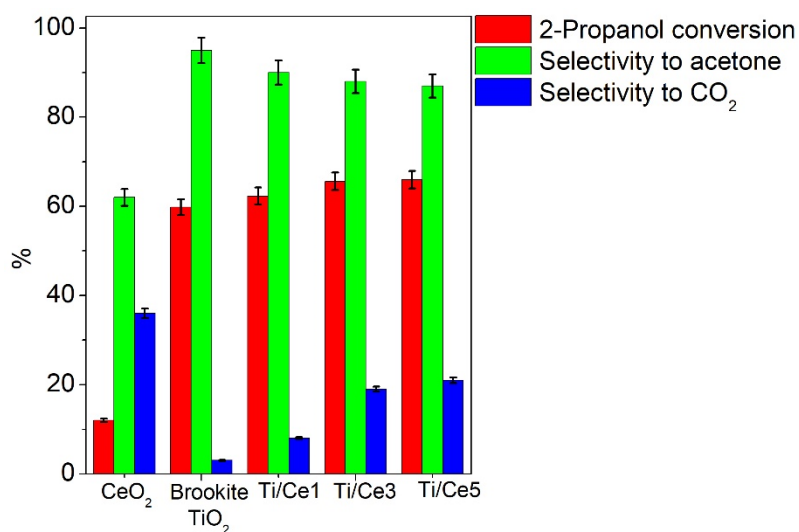
Figure 7. Photocatalytic oxidation of 2-propanol at room temperature, under simulated solar irradiation for 2 h over the investigated catalysts.

The synergism between TiO_2 and CeO_2 was even more exploited in the photo-thermo catalytic oxidation, i.e., with the contemporaneous use of the simulated solar irradiation and the thermal heating of the reactor. The thermal catalysis favored the total oxidization of the 2-propanol to CO_2, limiting the formation of acetone to a close range of temperatures, whereas the contemporaneous utilization of the solar light permitted to decrease the conversion temperatures. In particular, from Table 4 (conversion curves illustrated in the Figure S3) it is possible to note for all of the samples a decrease of the conversion temperatures with respect to the thermocatalytic tests (Table 3), most relevant for the mixed oxides catalysts. The T_{90} of brookite decreased by 40 °C and 20 °C for the 2-propanol conversion and for the conversion to CO_2, respectively; for the Ti/Ce1 the T_{90} decrease was of 48 °C for the alcohol conversion and 19 °C for the conversion to carbon dioxide. The Ti/Ce3 and the Ti/Ce5 composites showed a higher decrease of T_{90} (see Tables 3 and 4). The diminution was of about 60 °C (2-propanol conversion) and 70 °C (conversion to CO_2) for both samples. The positive effect of the photothermal approach was less effective for the bare CeO_2 (T_{90} diminution of 7 °C for the 2-propanol conversion and of 18 °C for the conversion to carbon dioxide).

Table 4. The photo-thermocatalytic oxidation of 2-propanol over the investigated samples.

Samples	2-Propanol Conversion	Conversion to CO_2	Maximum Conversion to Acetone
CeO_2	T_{10} = 281 °C T_{50} = 348 °C T_{90} = 407 °C	T_{10} = 374 °C T_{50} = 403 °C T_{90} = 416 °C	52% (367 °C)
Brookite TiO_2	T_{10} = 170 °C T_{50} = 192 °C T_{90} = 218 °C	T_{10} = 260 °C T_{50} = 282 °C T_{90} = 303 °C	96% (235 °C)
Ti/Ce1	T_{10} = 162 °C T_{50} = 178 °C T_{90} = 208 °C	T_{10} = 240 °C T_{50} = 265 °C T_{90} = 287 °C	97% (225 °C)
Ti/Ce3	T_{10} = 130 °C T_{50} = 152 °C T_{90} = 196 °C	T_{10} = 172 °C T_{50} = 200 °C T_{90} = 224 °C	61% (180 °C)
Ti/Ce5	T_{10} = 114 °C T_{50} = 151 °C T_{90} = 199 °C	T_{10} = 166 °C T_{50} = 187 °C T_{90} = 214 °C	57% (165 °C)

Another interesting effect verified with the multi catalytic approach was the increase of the maximum of acetone conversion occurring for all of the samples at a lower temperature in comparison to the thermocatalytic tests (see Tables 3 and 4). The presence of the solar radiation facilitated the 2-propanol conversion to acetone, as also detected in the photocatalytic test at room temperature (Figure 7). However, similarly to the thermocatalytic tests. the increase of cerium oxide in the composites decreased the maximum of acetone conversion, (from the 97% at 225 °C of Ti/Ce1 to the 57% at 165 °C of Ti/Ce5), confirming that the addition of ceria favors the 2-propanol conversion to CO_2 more than the conversion to acetone.
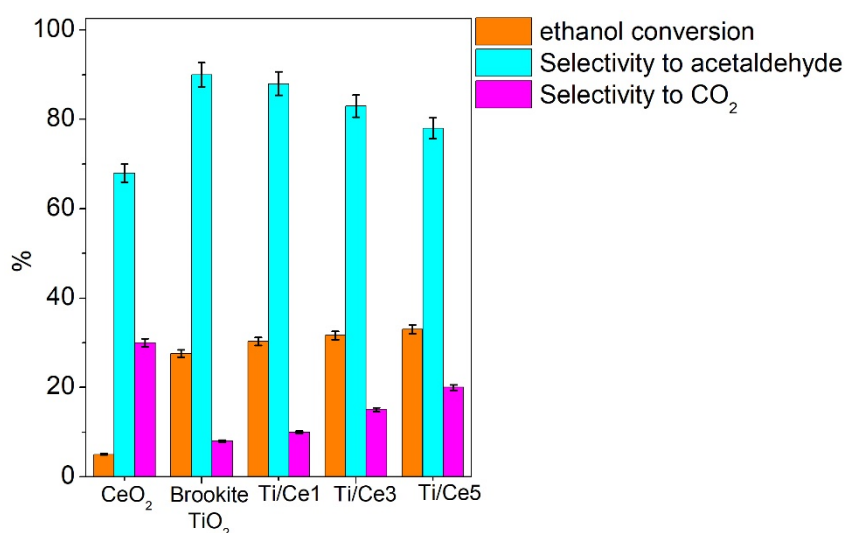
2.4. (Photo)Catalytic Oxidation of Ethanol

With respect to 2-propanol, ethanol, being a primary alcohol, required a higher temperature for the thermocatalytic oxidation (Table 5, Figure S4). In this case, acetaldehyde was the main intermediate. Similar to the 2-propanol thermocatalytic oxidation. the Ti/Ce5 and the Ti/Ce3 were the best active samples with the following order of activity both for the ethanol conversion and for the conversion to CO_2: Ti/Ce5 > Ti/Ce3 > Ti/Ce1 > TiO_2 > CeO_2.

The lowest T_{90} temperatures were obtained with the Ti/Ce5 sample (270 °C for the ethanol conversion and 292 °C for the conversion to CO_2). Moreover, also in this case the presence of cerium oxide favored the conversion to CO_2, and consequently the maximum of acetaldehyde conversion decreased from 69% at 271 °C with bare brookite to 41% at 232 °C with the TiCe/5 composite.

Table 5. Ethanol thermo-catalytic oxidation over the investigated samples.

Samples	Ethanol Conversion	Conversion to CO_2	Maximum Conversion to Acetaldehyde
CeO_2	T_{10} = 299 °C T_{50} = 347 °C T_{90} = 426 °C	T_{10} = 342 °C T_{50} = 393 °C T_{90} = 440 °C	38% (375 °C)
Brookite TiO_2	T_{10} = 244 °C T_{50} = 258 °C T_{90} = 290 °C	T_{10} = 279 °C T_{50} = 303 °C T_{90} = 330 °C	69% (271 °C)
Ti/Ce1	T_{10} = 222 °C T_{50} = 248 °C T_{90} = 284 °C	T_{10} = 273 °C T_{50} = 298 °C T_{90} = 327 °C	71% (268 °C)
Ti/Ce3	T_{10} = 218 °C T_{50} = 237 °C T_{90} = 274 °C	T_{10} = 232 °C T_{50} = 282 °C T_{90} = 315 °C	44% (271 °C)
Ti/Ce5	T_{10} = 187 °C T_{50} = 216 °C T_{90} = 270 °C	T_{10} = 208 °C T_{50} = 249 °C T_{90} = 292 °C	40% (232 °C)

Likewise, in the solar photocatalytic oxidation of ethanol (Figure 8) the conversion values were lower compared to those of 2-propanol. Similar to the previous cases. the main difference in the photocatalytic behavior of the composites compared to the bare brookite was the high selectivity to CO_2 that was 20% for the Ti/Ce5, 15% for the Ti/Ce3 and 10% for the Ti/Ce1, higher than that measured for the bare brookite (8%).

Figure 8. Photocatalytic oxidation of ethanol at room temperature, under simulated solar irradiation for 2 h over the investigated catalysts.

The lower acidity of ceria compared to that of TiO_2 [61–63] enhanced the formation of carbon dioxide, as also stated by the (photo)catalytic oxidation of 2-propanol. Indeed, similarly to the 2-propanol solar photocatalytic oxidation. the bare CeO_2 showed the highest CO_2 selectivity (30%) (Figure 8). In the same employed experimental conditions. the bare brookite exhibited higher ethanol photocatalytic conversion at room temperature (27%) with respect to P25 TiO_2 ($\approx$17%) and commercial anatase TiO_2 ($\approx$18%) [27,64].

In the photothermo-catalytic oxidation of ethanol (Table 6, Figure S5) a decrease of the conversion temperatures with respect to the thermocatalytic tests was detected. This diminution was lower compared to the 2-propanol photothermo-oxidation, but however, it was consistent especially in the samples with the highest amount of cerium oxide, confirming the occurrence of a synergism between the cerium oxide and the brookite TiO_2. The Ti/Ce5 catalyst showed a decrease of the T_{90} temperatures

of 44 °C for the alcohol conversion and of 42 °C for the conversion to CO_2. the Ti/Ce3 sample displayed a decrease of about 40 °C for both temperatures, whereas the diminution was less marked for the Ti/Ce1 and the bare brookite samples (decrease of $\approx$ 25 °C). Additionally, in this case, a contextual decrease of the temperature of maximum conversion to the intermediate was verified, whereas only a slight variation (temperatures decrease in the range 5–8 °C) was detected for the bare CeO_2.

Table 6. Ethanol photothermo-catalytic oxidation over the investigated samples.

| Samples	Ethanol Conversion	Conversion to CO_2	Maximum Conversion to Acetaldehyde
CeO_2	T_{10} = 294 °C T_{50} = 343 °C T_{90} = 418 °C	T_{10} = 337 °C T_{50} = 386 °C T_{90} = 435 °C	40% (360 °C)
Brookite TiO_2	T_{10} = 221 °C T_{50} = 236 °C T_{90} = 268 °C	T_{10} = 256 °C T_{50} = 279 °C T_{90} = 307 °C	68% (253 °C)
Ti/Ce1	T_{10} = 198 °C T_{50} = 224 °C T_{90} = 259 °C	T_{10} = 249 °C T_{50} = 273 °C T_{90} = 302 °C	72% (244 °C)
Ti/Ce3	T_{10} = 178 °C T_{50} = 197 °C T_{90} = 236 °C	T_{10} = 192 °C T_{50} = 242 °C T_{90} = 275 °C	43% (228 °C)
Ti/Ce5	T_{10} = 145 °C T_{50} = 174 °C T_{90} = 226 °C	T_{10} = 167 °C T_{50} = 207 °C T_{90} = 250 °C	39% (190 °C)

2.5. (Photo)Catalytic Oxidation of Toluene

To test the reactivity of the brookite TiO_2–CeO_2 composites towards aromatic VOCs. the thermocatalytic (Figure 9a), photocatalytic (Figure 9b) and photothermo-catalytic oxidation (Figure 9c) of toluene was investigated. As expected, due to the minor reactivity of the aromatic compounds with respect to the alcohols. the conversion temperatures for toluene were higher than those measured for the 2-propanol and ethanol oxidation [65,66]. In all experiments, including the solar photocatalytic tests at room temperature, only the CO_2 and water were detected with a very low selectivity (1–3%) to benzaldehyde [67–70]. The catalytic trend observed in the (photo)catalytic oxidation of alcohols was further confirmed in the toluene thermocatalytic oxidation with an order of activity that was Ti/Ce5 > Ti/Ce3 > Ti/Ce1 $\geq$ TiO_2 > CeO_2, with the most active catalysts (Ti/Ce5 and Ti/Ce1) exhibiting a T_{90} of 374 °C and 378 °C, respectively. Furthermore, in this case. the addition of cerium oxide had a beneficial effect. the T_{90} temperatures being lower compared to pure brookite (411 °C), whereas the Ti/Ce1 showed only a slightly better activity (T_{90} = 403 °C).

In the photocatalytic tests under solar irradiation (Figure 9b). the composites with the higher amount of cerium oxide improved the photoactivity of pure single oxides, although the degradation percentages were lower compared to the photoconversion of alcohols.

In the photothermo-catalytic tests (Figure 9c) with the Ti/Ce5 and the Ti/Ce3 samples, a decrease of the T_{90} temperature compared to the thermal catalytic tests of about 20 °C and 13 °C was verified, respectively, whereas in the other samples. the decrease of the conversion temperatures was smaller.

To have a general idea of the catalytic stability of the TiCe/5 after the photothermo oxidation of toluene (as stated before the most difficult VOC to oxidize among those used in this work). the toluene conversion was measured after long-time on-stream measurements at T = 350 °C (i.e.. the T_{90} of the sample, Figure 10a) and after five consecutive runs (Figure 10b). Only a little decrease from 90% to 84% of toluene conversion was measured after 45 h of the test, and also a little shift of T_{90} at a higher temperature (about 8 °C) was verified after five consecutive runs, pointing to the discrete stability of the investigated composite.
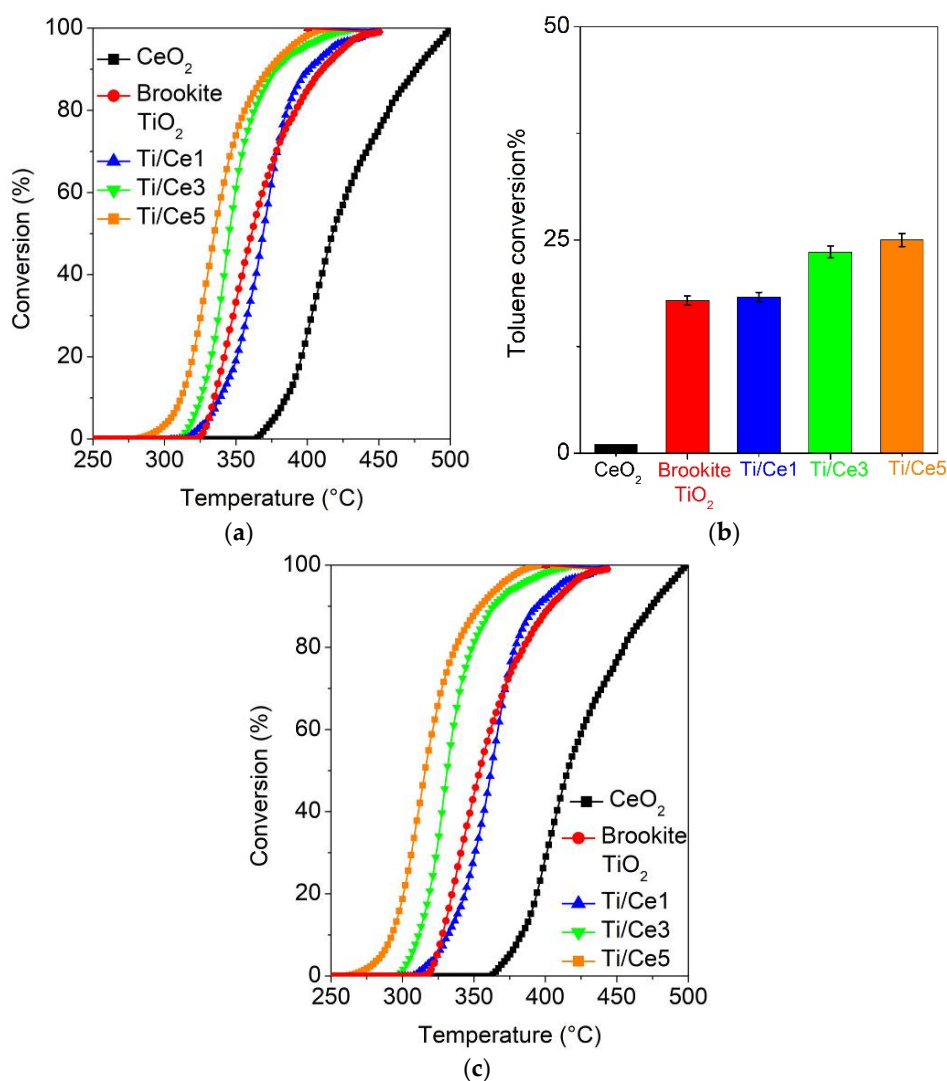
Figure 9. (**a**) Toluene thermocatalytic oxidation; (**b**) solar photocatalytic oxidation at room temperature after 2 h of irradiation; and (**c**) the photothermo-catalytic oxidation on the investigated samples.
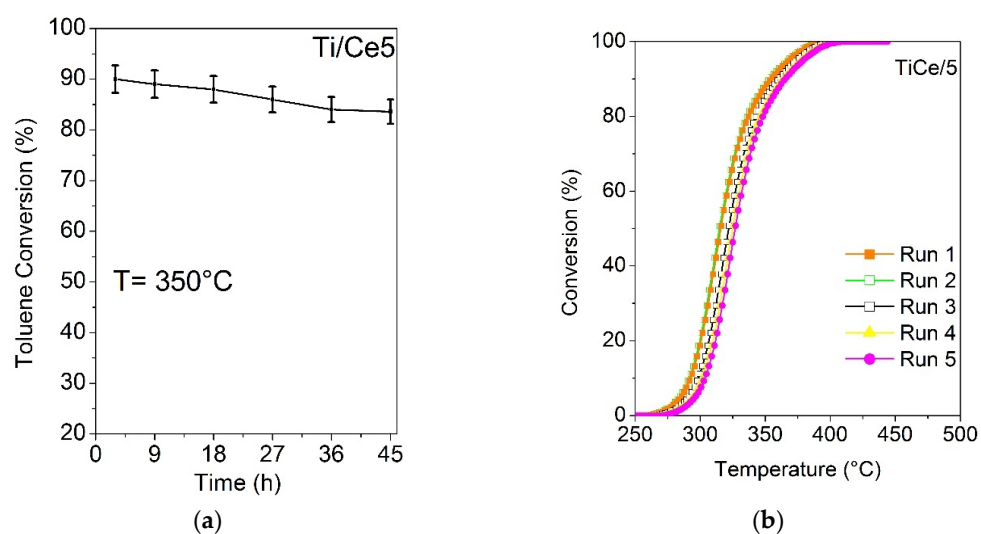
Figure 10. Photothermo-catalytic oxidation of toluene on the Ti/Ce5 composite: (**a**) the variation in the toluene conversion after a long-time on-stream test; and (**b**) the toluene conversion curves after 5 consecutive runs.

The XPS results after the photothermo catalytic oxidation of 2-propanol (as representative alcohol) and after the long-time on-stream toluene tests of the Ti/Ce5 sample showed no significant variations (Figure S6) in the Ce 3d and Ti 2p regions compared to the sample analyzed before the catalytic tests. In the O 1s and C 1s regions, a small contribution ascribed to the carbonation process was verified after the toluene tests, and reasonably the occurrence of this process can be the cause of the little decrease of the conversion values after a long time and consecutive tests of toluene photothermo-catalytic oxidation.
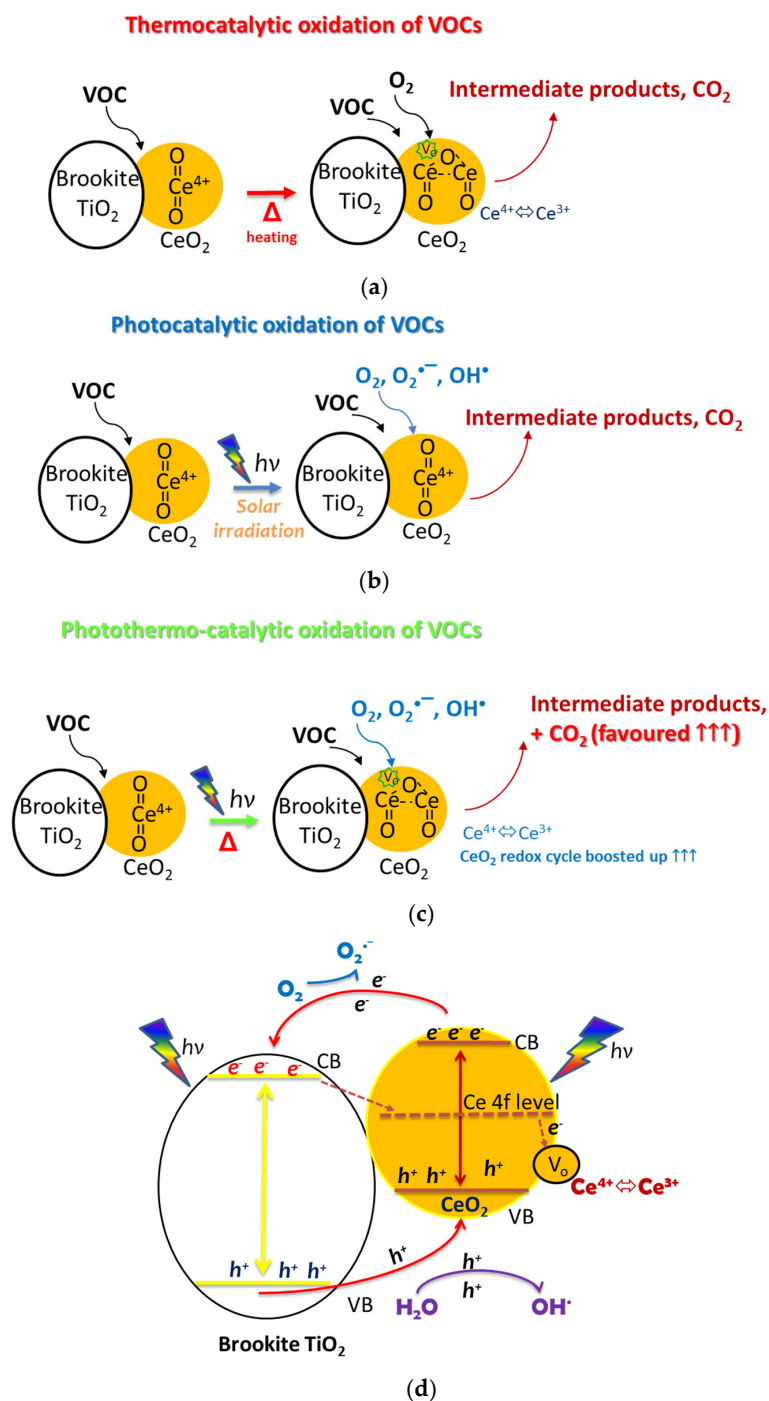
2.6. Photothermo-Catalytic Mechanisms

The (photo)catalytic data of the VOC oxidation have shown as the main result that the addition of even small amounts of cerium oxide in brookite TiO_2 has led to an increase in activity, with also an improvement in the formation of CO_2. The good affinity between TiO_2 and CeO_2 was further exploited in the photothermo-catalytic tests, where the synergism between the catalytic and the photocatalytic mechanism also played a crucial role.

Indeed. the thermo-driven oxidation of VOCs, with reducible oxides (as CeO_2) followed a Mars–van Krevelen (MvK) redox mechanism, where the surface reducible oxygens of the employed catalyst directly participate in the oxidation of the organic compound, facilitating the total oxidation to CO_2 [17,71]. In particular, for the CeO_2-based catalyst. the high reactivity of its oxygens was strictly connected with its redox properties: the $Ce^{4+} \rightarrow Ce^{3+}$ reduction releases oxygens (that will oxidize the VOC) with a consequent formation of oxygen vacancies in the ceria lattice. These vacancies will be successively filled by oxygens in the gas phase, thus exploiting the redox properties of cerium oxide [23,72] (Figure 11a). In the photocatalytic oxidation of VOCs with semiconductor catalysts. the generation of highly reactive species as the hydroxide and the superoxide radicals after the irradiation of the photoactive materials allows to degrade the dangerous pollutants [73,74] (Figure 11b).

In our case, in the thermocatalytic tests. the good interaction between titania and ceria permitted to increase the performance compared to the single oxides, whereas when the photo-oxidation route was also activated. the presence of the oxygen radicals boosted up the total oxidation of VOCs, simultaneously favoring the redox cycle of CeO_2 [18,23,32,36] (Figure 11c). Indeed. the oxygen radicals, more reactive compared to the oxygen in the gas phase, interact with the cerium oxide surface, accelerating its redox cycle [19,75]. Therefore. the redox process on the cerium oxide is speeded up in the photothermo-catalytic tests. The solar light-driven photothermo-catalytic oxidation rate of VOCs was in this way significantly enhanced, thus explaining the decrease of the conversion temperatures with respect to the thermocatalytic tests, observed for all of the composite materials. This strong affinity between the TiO_2 and CeO_2 strongly affected the selectivity of products after the (photo)catalytic oxidation of VOCs. Indeed, whereas with the bare brookite. the partial oxidation of alcohols was favored (Tables 3–6, Figures 7 and 8), a crescent amount of cerium oxide allowed to increase the selectivity to CO_2, facilitating the total oxidation of VOCs. This catalytic behavior was further promoted in the photothermal tests and in the oxidation of toluene where no intermediate products were formed. With the TiO_2-CeO_2 composites, it was possible to exploit a double effect: the photoactivity of TiO_2 allowed to start the oxidation of VOCs, whereas the redox properties of CeO_2 boosted up the VOC conversion towards the total oxidation to CO_2.

The occurrence of this mutual synergism between the brookite TiO_2 and the CeO_2 was also confirmed by XPS. This strong interaction in fact favored the formation of the Ce^{3+} species increasing the amount of cerium oxide in the brookite. This feature is advantageous for the thermo-catalytic and even more for the photothermo-catalytic reactions, since the redox cycle of ceria was even more promoted by the continuous interaction with TiO_2, thus explaining the higher activity of the Ti/Ce3 and Ti/Ce5 samples. Although the bare CeO_2 showed the lowest optical band-gap (2.87 instead of the 3.22 eV of brookite), only the combination with brookite allowed to increase its photocatalytic performance. The good dispersion of ceria in the TiO_2, and the formation of an efficient heterojunction between the two oxides (as verified by the Raman and HRTEM characterizations) resulted in an improvement of the charge carrier separation, as confirmed by the PL measurements, that allowed to

efficiently activate the photo-oxidation mechanism. Moreover, with the multi catalytic approach and the contemporary exploitation of the photocatalytic properties of brookite and the redox properties of the ceria. the TiO_2-photogenerated electrons can be moved to the empty 4f energy levels of CeO_2 or can be trapped by the ceria oxygen vacancies that are formed during the oxidation reactions, further increasing the separation of the charge carriers, and simultaneously promoting the oxidation of VOCs by the titania and ceria photoholes [76] (Figure 11d).

Figure 11. Reaction scheme of (**a**) the thermocatalytic oxidation of the volatile organic compounds (VOCs); (**b**) the photocatalytic oxidation of VOCs; (**c**) the photothermo-catalytic oxidation of VOCs, (**d**) the charge carrier separation on the brookite TiO_2–CeO_2 composites. V_o represents an oxygen vacancy.

In this context. the utilization of brookite was advantageous because a moderate depth of photoelectron trap with respect to anatase or rutile TiO_2 was reported, and consequently both the electrons and holes are highly reactive [31,77]. This is beneficial for the oxidation of VOCs because the residual free photoelectrons of brookite can reduce the gas-phase oxygens to further increase the formation of superoxide radicals that in turn can re-oxidize the cerium oxide, enhancing in this way the overall performance of the brookite TiO_2-CeO_2 composite.

The combination of the peculiar photocatalytic properties of brookite TiO_2 together with the redox properties of CeO_2 activated with a multi-catalytic approach can be a fascinating strategy to increase the efficiency of the catalytic VOC degradation.

3. Materials and Methods

3.1. Catalysts Synthesis

Brookite TiO_2 was synthesized with the thermohydrolysis of titanium tetrachloride in a hydrochloric acid-concentrated solution as reported in the refs. [28,29]. Briefly, 5 mL of titanium tetrachloride (98% Fluka) were slowly adjunct to a 210 mL of H_2O and 80 mL of hydrochloric acid. After heating the solution in a closed reactor, it was transferred to the oven and aged at 100 °C for 48 h. The obtained brookite-rutile mixture was washed to remove the supernatant and to separate the brookite phase. The drying under vacuum at 55 °C was the final step of the synthesis.

The wetness impregnation was used on the as-synthetized brookite to obtain the composites with different (1, 3, and 5) weight percentages (wt%) of CeO_2. In particular, a solution of cerium nitrate hexahydrate (Fluka, Buchs, Switzerland), was added towards impregnation to the brookite, and the obtained slurry was dried at 120 °C and calcined at 350 °C for 4 h.

The bare CeO_2 was synthetized through the chemical precipitation with KOH (Fluka, Buchs, Switzerland) following the procedure reported in the refs. [20,78]. After digestion and filtration. the same thermal treatments described above (drying at 120 °C and calcination at 350 °C) were used.

3.2. Characterization Measurements

Raman characterizations were performed using a WITec alpha 300 confocal Raman instrument (WITec Wissenschaftliche Instrumente und Technologie GmbH, Ulm, Germany) exciting at 532, and the details of the configuration are reported in the ref. [18].

The HRTEM measurements were made with a JEOL JEM 2100F (JEOL Europe SAS, Allée de Giverny, France) working at 200 kV.

N_2 adsorption–desorption measurements were accomplished utilizing a Sorptomatic series 1990 instrument (Thermo Quest, Milano, Italy). The samples were pre-treated with an outgassing step at 100 °C for 12 h.

The UV-vis Diffuse Reflectance Spectroscopy (UV-Vis DRS (Diffuse Reflectance Spectroscopy)) measurements were carried with a Cary 60 spectrometer (Agilent Stevens Creek Blvd. Santa Clara, CA, USA).

Photoluminescence (PL) spectra were obtained by means of a Horiba Jobin Yvon spectrofluorometer (FluoroMax-4, Horiba UK Limited, Kyoto Close, Moulton ParkNorthamptonNN3 6FL, United Kingdom). The spectra were obtained with an excitation energy of 300 nm.

X-ray photoelectron spectra (XPS) were performed with a PHI 5600 Multi Technique System (Physical Electronics GmbH, Feldkirchen, Germany, base pressure of the main chamber 1×10^{-8} Pa, instrumental energy resolution < 0.4 eV) adopting the experimental conditions reported in the ref. [79,80]. The samples were excited with Al Kα X-ray radiation using a pass energy of 5.85 eV. The calibration was set on C 1s signal at 285.0 eV and the intensity of peaks plotted after a Shirley background removal [81]. The fitting of the Ce 3d XP spectrum was performed, following the procedure reported in the ref. [82].

The surface atomic concentration of the sample was calculated considering the relevant atomic sensitivity factors. It should be noted that considering the surface XPS measured concentrations. the so-called 1, 3 and 5 % TiO_2-CeO_2 samples refer to the weight nominal composition, while in terms of atomic concentrations, these values turn in 0.47, 1.41 and 2.38%, respectively.

3.3. (Photo)Catalytic Measurements

The gas-phase thermo-catalytic oxidation of VOCs was performed continuously in a flow reactor packed with the powder sample (P = 1 atm, 150 mg, 80–140 mesh) employing the reaction conditions reported in the ref. [27]. For each test, a ramp with a rate of 10 °C/min was used (from room temperature to 500 °C). The reactant mixture was adsorbed–desorbed over the catalyst (0.1 vol.% VOCs; 10 vol.% air, rest He) for 30 min to assure the steady-state before starting with the analyses. The products were examined online by a gas chromatography (Smart-IQ$^+$ Thermo Onix, Thermo Fisher Scientific 168 Third Avenue, Waltham, MA USA 0245) utilizing a packed column with 10% FFAP on Chromosorb W (from Merck KGaA, Darmstadt, Germany) with a FID (Flame Ionization Detector), coupled with a quadrupole mass spectrometer (VG quadropoles, Fergutec B.V. Dragonder 13C, 5554 GM Valkenswaard, The Netherlands).

The photothermo-catalytic measurements were carried out with the same instruments described above, contextually heating the reactor and irradiating it with an artificial solar lamp (OSRAM Vitalux 300W, OSRAM Opto Semiconductors GmbH, Leibniz, Regensburg Germany). A water jacket surrounding the solar lamp was used to avoid the simultaneous heating due to the continuous emission of the lamp.

The photocatalytic experiments at room temperature were carried out irradiating the reactor for 2 h with the artificial solar lamp, using the refrigeration water jacket and the experimental setup described above. In our experimental conditions. the conversion and selectivities were reproducible within the 3%.

4. Conclusions

The (photo)catalytic abatement of VOCs was investigated through a multi-catalytic approach.

The combination between thermocatalysis and photocatalysis permitted to exploit the two oxidation mechanisms, and the addition of cerium oxide to the brookite TiO_2 allowed to sensibly increase the catalytic activity of the bare oxides. The presence of a small amount of ceria (1, 3 and 5 wt%) on brookite TiO_2 led to a reduction of the recombination rate between the charge carriers, producing a substantial decrease of the VOCs conversion temperatures also favoring the combustion of dangerous organic compounds to CO_2. The solar driven-photothermo-catalytic oxidation of VOCs with semiconductor composites is a simple, green and charming strategy for the removal of these hazardous compounds from both the indoor and outdoor living environment.

Conflicts of Interest: The authors declare no conflict of interest.

References

1. Shah, K.W.; Li, W. A review on catalytic nanomaterials for volatile organic compounds VOC removal and their applications for healthy buildings. *Nanomaterials* **2019**, *9*, 910. [CrossRef]

2. Bautista-Gutierrez, K.P.; Herrera-May, A.L.; Santamaría-López, J.M.; Honorato-Moreno, A.; Zamora-Castro, S.A. Recent progress in nanomaterials for modern concrete infrastructure: Advantages and challenges. *Materials (Basel)* **2019**, *12*, 3458. [CrossRef]

3. Truppi, A.; Petronella, F.; Placido, T.; Striccoli, M.; Agostiano, A.; Curri, M.L.; Comparelli, R. Visible-light-active TiO$_2$-based hybrid nanocatalysts for environmental applications. *Catalysts* **2017**, *7*, 100. [CrossRef]

4. Varma, A.; James, A.R.; Daniel, S.A. A Review on Nano TiO$_2$—A Repellent in Paint. In *Lecture Notes in Civil Engineering*; Springer Nature Switzerland AG: Charm, Switzerland, 2020; Volume 46, pp. 908–919.

5. Hamidi, F.; Aslani, F. TiO$_2$-based photocatalytic cementitious composites: Materials, properties, influential parameters, and assessment techniques. *Nanomaterials* **2019**, *9*, 1444. [CrossRef]

6. Enea, D.; Bellardita, M.; Scalisi, P.; Alaimo, G.; Palmisano, L. Effects of weathering on the performance of self-cleaning photocatalytic paints. *Cem. Concr. Compos.* **2019**, *96*, 77–86. [CrossRef]

7. Katal, R.; Masudy-Panah, S.; Tanhaei, M.; Farahani, M.H.D.A.; Jiangyong, H. A review on the synthesis of the various types of anatase TiO$_2$ facets and their applications for photocatalysis. *Chem. Eng. J.* **2020**, *384*, 123384. [CrossRef]

8. Al Jitan, S.; Palmisano, G.; Garlisi, C. Synthesis and surface modification of TiO$_2$-based photocatalysts for the conversion of CO$_2$. *Catalysts* **2020**, *10*, 227. [CrossRef]

9. Karthikeyan, C.; Arunachalam, P.; Ramachandran, K.; Al-Mayouf, A.M.; Karuppuchamy, S. Recent advances in semiconductor metal oxides with enhanced methods for solar photocatalytic applications. *J. Alloys Compd.* **2020**, *828*, 154281. [CrossRef]

10. Fiorenza, R.; Sciré, S.; D'Urso, L.; Compagnini, G.; Bellardita, M.; Palmisano, L. Efficient H$_2$ production by photocatalytic water splitting under UV or solar light over variously modified TiO$_2$-based catalysts. *Int. J. Hydrogen Energy* **2019**, *44*, 14796–14807. [CrossRef]

11. Fujishima, A.; Rao, T.N.; Tryk, D.A. Titanium dioxide photocatalysis. *J. Photochem. Photobiol. C Photochem. Rev.* **2000**, *1*, 1–21. [CrossRef]

12. Di Paola, A.; Bellardita, M.; Palmisano, L. Brookite. the Least Known TiO$_2$ Photocatalyst. *Catalysts* **2013**, *3*, 36–73. [CrossRef]

13. Liu, L.; Zhao, H.; Andino, J.M.; Li, Y. Photocatalytic CO$_2$ Reduction with H$_2$O on TiO$_2$ Nanocrystals: Comparison of Anatase, Rutile, and Brookite Polymorphs and Exploration of Surface Chemistry. *ACS Catal.* **2012**, *2*, 1817–1828. [CrossRef]

14. Ramos-Delgado, N.A.; Hinojosa-Reyes, L.; Guzman-Mar, I.L.; Gracia-Pinilla, M.A.; Hernández-Ramírez, A. Synthesis by sol–gel of WO$_3$/TiO$_2$ for solar photocatalytic degradation of malathion pesticide. *Catal. Today* **2013**, *209*, 35–40. [CrossRef]

15. Kum, J.M.; Yoo, S.H.; Ali, G.; Cho, S.O. Photocatalytic hydrogen production over CuO and TiO$_2$ nanoparticles mixture. *Int. J. Hydrogen Energy* **2013**, *38*, 13541–13546. [CrossRef]

16. Sood, S.; Mehta, S.K.; Sinha, A.S.K.; Kansal, S.K. Bi$_2$O$_3$/TiO$_2$ heterostructures: Synthesis, characterization and their application in solar light mediated photocatalyzed degradation of an antibiotic, ofloxacin. *Chem. Eng. J.* **2016**, *290*, 45–52. [CrossRef]

17. Bellardita, M.; Fiorenza, R.; Palmisano, L.; Scirè, S. Photocatalytic and photothermocatalytic applications of cerium oxide-based materials. In *Cerium Oxide (CeO$_2$): Synthesis, Properties and Applications*; Elsevier: Amsterdam, The Netherlands, 2020; pp. 109–167. Available online: https://scholar.google.com/scholar?hl=it&as_sdt=0%2C5&q=Photocatalytic+and+photothermocatalytic+applications+of+cerium+oxide-based+materials.+In+Cerium+Oxide+%28CeO2+%29%3A+Synthesis%2C+Properties+and+Applications%3B+Elsevier%3A+Amsterdam%2C+The+Netherlands%2C+2020%3B+pp.+109%E2%80%93167.+Google+scholar%3A+&btnG= (accessed on 7 July 2020).

18. Fiorenza, R.; Bellardita, M.; D'Urso, L.; Compagnini, G.; Palmisano, L.; Scirè, S. Au/TiO$_2$-CeO$_2$ catalysts for photocatalytic water splitting and VOCs oxidation reactions. *Catalysts* **2016**, *6*, 121. [CrossRef]

19. Sciré, S.; Palmisano, L. *Cerium Oxide (CeO$_2$): Synthesis, Properties and Applications*; Elsevier: Amsterdam, The Netherlands, 2020; ISBN 9780128156612. Available online: https://scholar.google.com/scholar?hl=it&as_sdt=0%2C5&q=Scir%C3%A9%2C+S.%3B+Palmisano%2C+L.+Cerium+Oxide+%28CeO2+%29%3A+Synthesis%2C+Properties+and+Applications%3B+Elsevier%3A+Amsterdam%2C+The+Netherlands%2C+2020%3B+ISBN+9780128156612.&btnG= (accessed on 7 July 2020).

20. Fiorenza, R.; Balsamo, S.A.; D'Urso, L.; Sciré, S.; Brundo, M.V.; Pecoraro, R.; Scalisi, E.M.; Privitera, V.; Impellizzeri, G. CeO$_2$ for Water Remediation: Comparison of Various Advanced Oxidation Processes. *Catalysts* **2020**, *10*, 446. [CrossRef]

21. Liu, B.; Zhao, X.; Zhang, N.; Zhao, Q.; He, X.; Feng, J. Photocatalytic mechanism of TiO2–CeO2 films prepared by magnetron sputtering under UV and visible light. *Surf. Sci.* **2005**, *595*, 203–211. [CrossRef]

22. Galindo, F.; Gómez, R.; Aguilar, M. Photodegradation of the herbicide 2,4-dichlorophenoxyacetic acid on nanocrystalline TiO2–CeO2 sol–gel catalysts. *J. Mol. Catal. A Chem.* **2008**, *281*, 119–125. [CrossRef]

23. Fiorenza, R.; Bellardita, M.; Palmisano, L.; Scirè, S. A comparison between photocatalytic and catalytic oxidation of 2-Propanol over Au/TiO$_2$-CeO$_2$ catalysts. *J. Mol. Catal. A Chem.* **2016**, *415*, 56–64. [CrossRef]

24. Montecchio, F.; Persson, H.; Engvall, K.; Delin, J.; Lanza, R. Development of a stagnation point flow system to screen and test TiO 2 -based photocatalysts in air purification applications. *Chem. Eng. J.* **2016**, *306*, 734–744. [CrossRef]

25. Boyjoo, Y.; Sun, H.; Liu, J.; Pareek, V.K.; Wang, S. A review on photocatalysis for air treatment: From catalyst development to reactor design. *Chem. Eng. J.* **2017**, *310*, 537–559. [CrossRef]

26. Vikrant, K.; Park, C.M.; Kim, K.H.; Kumar, S.; Jeon, E.C. Recent advancements in photocatalyst-based platforms for the destruction of gaseous benzene: Performance evaluation of different modes of photocatalytic operations and against adsorption techniques. *J. Photochem. Photobiol. C Photochem. Rev.* **2019**, *41*, 100316. [CrossRef]

27. Fiorenza, R.; Condorelli, M.; D'Urso, L.; Compagnini, G.; Bellardita, M.; Palmisano, L.; Scirè, S. Catalytic and photothermo-catalytic applications of TiO2-CoOx composites. *J. Photocatal.* **2020**, *1*, 1–13. [CrossRef]

28. Di Paola, A.; Cufalo, G.; Addamo, M.; Bellardita, M.; Campostrini, R.; Ischia, M.; Ceccato, R.; Palmisano, L. Photocatalytic activity of nanocrystalline TiO2 (brookite, rutile and brookite-based) powders prepared by thermohydrolysis of TiCl4 in aqueous chloride solutions. *Colloids Surfaces A Physicochem. Eng. Asp.* **2008**, *317*, 366–376. [CrossRef]

29. Bellardita, M.; Di Paola, A.; Megna, B.; Palmisano, L. Absolute crystallinity and photocatalytic activity of brookite TiO2 samples. *Appl. Catal. B Environ.* **2017**, *201*, 150–158. [CrossRef]

30. Tompsett, G.A.; Bowmaker, G.A.; Cooney, R.P.; Metson, J.B.; Rodgers, K.A.; Seakins, J.M. The Raman spectrum of brookite, TiO$_2$ (Pbca, Z = 8). *J. Raman Spectrosc.* **1995**, *26*, 57–62. [CrossRef]

31. Monai, M.; Montini, T.; Fornasiero, P. Brookite: Nothing new under the sun? *Catalysts* **2017**, *7*, 304. [CrossRef]

32. Fiorenza, R.; Bellardita, M.; Barakat, T.; Scirè, S.; Palmisano, L. Visible light photocatalytic activity of macro-mesoporous TiO$_2$-CeO$_2$ inverse opals. *J. Photochem. Photobiol. A Chem.* **2018**, *352*, 25–34. [CrossRef]

33. Wang, Y.; Zou, Y.; Shang, Q.; Tan, X.; Yu, T.; Huang, X.; Shi, W.; Xie, Y.; Yan, G.; Wang, X. Quasi-Spherical Brookite TiO2 Nanostructures Synthesized Using Solvothermal Method in the Presence of Oxalic Acid. *Trans. Tianjin Univ.* **2018**, *24*, 326–339. [CrossRef]

34. Su, W.; Zhang, J.; Feng, Z.; Chen, T.; Ying, P.; Li, C. Surface Phases of TiO 2 Nanoparticles Studied by UV Raman Spectroscopy and FT-IR Spectroscopy. *J. Phys. Chem. C* **2008**, *112*, 7710–7716. [CrossRef]

35. Choudhury, B.; Borah, B.; Choudhury, A. Ce–Nd codoping effect on the structural and optical properties of TiO2 nanoparticles. *Mater. Sci. Eng. B* **2013**, *178*, 239–247. [CrossRef]

36. Zeng, M.; Li, Y.; Mao, M.; Bai, J.; Ren, L.; Zhao, X. Synergetic Effect between Photocatalysis on TiO_2 and Thermocatalysis on CeO2 for Gas-Phase Oxidation of Benzene on TiO_2/CeO_2 Nanocomposites. *ACS Catal.* **2015**, *5*, 3278–3286. [CrossRef]

37. Pigeot-Rémy, S.; Gregori, D.; Hazime, R.; Hérissan, A.; Guillard, C.; Ferronato, C.; Cassaignon, S.; Colbeau-Justin, C.; Durupthy, O. Size and shape effect on the photocatalytic efficiency of TiO_2 brookite. *J. Mater. Sci.* **2019**, *54*, 1213–1225. [CrossRef]

38. Sing, K.S.W. Reporting physisorption data for gas/solid systems with special reference to the determination of surface area and porosity (Recommendations 1984). *Pure Appl. Chem.* **1985**, *57*, 603–619. [CrossRef]

39. Shen, X.; Tian, B.; Zhang, J. Tailored preparation of titania with controllable phases of anatase and brookite by an alkalescent hydrothermal route. *Catal. Today* **2013**, *201*, 151–158. [CrossRef]

40. Wei, X.; Lü, X.; Wu, Z.; Ding, J.; Xie, J.; Wei, W.; Mao, D. Reactivity and mechanistic insight into visible-light-induced anerobic selective reaction by Ag/brookite titania. *J. Nanosci. Nanotechnol.* **2012**, *12*, 8017–8022. [CrossRef]

41. Asadollahi, E.; Youzbashi, A.A.; Keyanpour-Rad, M. Synthesis and investigation of crystal structure and optical properties of brookite TiO_2 nanoparticles capped with (2-chloroquinoline-3-yl) methanol. *J. Mol. Struct.* **2017**, *1128*, 612–618. [CrossRef]

42. Yamashita, H.; Harada, M.; Misaka, J.; Takeuchi, M.; Neppolian, B.; Anpo, M. Photocatalytic degradation of organic compounds diluted in water using visible light-responsive metal ion-implanted TiO_2 catalysts: Fe ion-implanted TiO_2. *Catal. Today* **2003**, *84*, 191–196. [CrossRef]

43. Yu, J.; Yue, L.; Liu, S.; Huang, B.; Zhang, X. Hydrothermal preparation and photocatalytic activity of mesoporous Au–TiO_2 nanocomposite microspheres. *J. Colloid Interface Sci.* **2009**, *334*, 58–64. [CrossRef]

44. Liqiang, J.; Yichun, Q.; Baiqi, W.; Shudan, L.; Baojiang, J.; Libin, Y.; Wei, F.; Honggang, F.; Jiazhong, S. Review of photoluminescence performance of nano-sized semiconductor materials and its relationships with photocatalytic activity. *Sol. Energy Mater. Sol. Cells* **2006**, *90*, 1773–1787. [CrossRef]

45. Xie, J.; Lü, X.; Liu, J.; Shu, H. Brookite titania photocatalytic nanomaterials: Synthesis, properties, and applications. *Pure Appl. Chem.* **2009**, *81*, 2407–2415. [CrossRef]

46. Lei, Y.; Zhang, L.D.; Meng, G.W.; Li, G.H.; Zhang, X.Y.; Liang, C.H.; Chen, W.; Wang, S.X. Preparation and photoluminescence of highly ordered TiO2 nanowire arrays. *Appl. Phys. Lett.* **2001**, *78*, 1125–1127. [CrossRef]

47. Gao, X.; Jiang, Y.; Zhong, Y.; Luo, Z.; Cen, K. The activity and characterization of CeO_2-TiO_2 catalysts prepared by the sol–gel method for selective catalytic reduction of NO with NH3. *J. Hazard. Mater.* **2010**, *174*, 734–739. [CrossRef] [PubMed]

48. Fang, J.; Bi, X.; Si, D.; Jiang, Z.; Huang, W. Spectroscopic studies of interfacial structures of CeO_2–TiO_2 mixed oxides. *Appl. Surf. Sci.* **2007**, *253*, 8952–8961. [CrossRef]

49. Gulino, A.; Taverner, A.E.; Warren, S.; Harris, P.; Egdell, R.G. A photoemission study of Sb-doped TiO_2. *Surf. Sci.* **1994**, *315*, 351–361. [CrossRef]

50. Qiu, L.; Liu, F.; Zhao, L.; Ma, Y.; Yao, J. Comparative XPS study of surface reduction for nanocrystalline and microcrystalline ceria powder. *Appl. Surf. Sci.* **2006**, *252*, 4931–4935. [CrossRef]

51. Bêche, E.; Charvin, P.; Perarnau, D.; Abanades, S.; Flamant, G. Ce 3d XPS investigation of cerium oxides and mixed cerium oxide (CexTiyOz). *Surf. Interface Anal.* **2008**, *40*, 264–267. [CrossRef]

52. Ji, P.; Zhang, J.; Chen, F.; Anpo, M. Ordered Mesoporous CeO_2 Synthesized by Nanocasting from Cubic Ia3d Mesoporous MCM-48 Silica: Formation, Characterization and Photocatalytic Activity. *J. Phys. Chem. C* **2008**, *112*, 17809–17813. [CrossRef]

53. Watanabe, S.; Ma, X.; Song, C. Characterization of Structural and Surface Properties of Nanocrystalline TiO2−CeO 2 Mixed Oxides by XRD, XPS, TPR, and TPD. *J. Phys. Chem. C* **2009**, *113*, 14249–14257. [CrossRef]

54. Eriksen, S.; Egdell, R.G. Electronic excitations at oxygen deficient TiO_2(110) surfaces: A study by EELS. *Surf. Sci.* **1987**, *180*, 263–278. [CrossRef]

55. Bharti, B.; Kumar, S.; Lee, H.-N.; Kumar, R. Formation of oxygen vacancies and Ti3+ state in TiO2 thin film and enhanced optical properties by air plasma treatment. *Sci. Rep.* **2016**, *6*, 32355. [CrossRef] [PubMed]

56. Cafun, J.-D.; Kvashnina, K.O.; Casals, E.; Puntes, V.F.; Glatzel, P. Absence of Ce 3+ Sites in Chemically Active Colloidal Ceria Nanoparticles. *ACS Nano* **2013**, *7*, 10726–10732. [CrossRef]

57. Tanner, P.A.; Mak, C.S.K.; Edelstein, N.M.; Murdoch, K.M.; Liu, G.; Huang, J.; Seijo, L.; Barandiarán, Z. Absorption and Emission Spectra of Ce3+ in Elpasolite Lattices. *J. Am. Chem. Soc.* **2003**, *125*, 13225–13233. [CrossRef] [PubMed]

58. Holz, M.C.; Kähler, K.; Tölle, K.; van Veen, A.C.; Muhler, M. Gas-phase oxidation of 2-propanol over Au/TiO2 catalysts to probe metal-support interactions. *Phys. Status Solidi* **2013**, *250*, 1094–1106. [CrossRef]

59. Sboui, M.; Bouattour, S.; Liotta, L.F.; La Parola, V.; Gruttadauria, M.; Marcì, G.; Boufi, S. Paper-TiO$_2$ composite: An effective photocatalyst for 2-propanol degradation in gas phase. *J. Photochem. Photobiol. A Chem.* **2018**, *350*, 142–151. [CrossRef]

60. García-López, E.I.; Marcì, G.; Dozzi, M.V.; Palmisano, L.; Selli, E. Photoactivity of shape-controlled TiO2 in gas-solid regime under solar irradiation. *Catal. Today* **2019**, *328*, 118–124. [CrossRef]

61. Godoi, D.R.M.; Villullas, H.M.; Zhu, F.-C.; Jiang, Y.-X.; Sun, S.-G.; Guo, J.; Sun, L.; Chen, R. A comparative investigation of metal-support interactions on the catalytic activity of Pt nanoparticles for ethanol oxidation in alkaline medium. *J. Power Sources* **2016**, *311*, 81–90. [CrossRef]

62. Liu, S.Y.; Yang, S.M. Complete oxidation of 2-propanol over gold-based catalysts supported on metal oxides. *Appl. Catal. A Gen.* **2008**, *334*, 92–99. [CrossRef]

63. Haffad, D.; Chambellan, A.; Lavalley, J.C. Propan-2-ol transformation on simple metal oxides TiO2, ZrO2 and CeO2. *J. Mol. Catal. A Chem.* **2001**, *168*, 153–164. [CrossRef]

64. Fiorenza, R.; Bellardita, M.; Scirè, S.; Palmisano, L. Effect of the addition of different doping agents on visible light activity of porous TiO$_2$ photocatalysts. *Mol. Catal.* **2018**, *455*, 108–120. [CrossRef]

65. O'Malley, A.; Hodnett, B.K. The influence of volatile organic compound structure on conditions required for total oxidation. *Catal. Today* **1999**, *54*, 31–38. [CrossRef]

66. Baldi, M.; Finocchio, E.; Milella, F.; Busca, G. Catalytic combustion of C3 hydrocarbons and oxygenates over Mn3O4. *Appl. Catal. B Environ.* **1998**, *16*, 43–51. [CrossRef]

67. Scirè, S.; Minicò, S.; Crisafulli, C.; Satriano, C.; Pistone, A. Catalytic combustion of volatile organic compounds on gold/cerium oxide catalysts. *Appl. Catal. B Environ.* **2003**, *40*, 43–49. [CrossRef]

68. Maira, A.J.; Yeung, K.L.; Soria, J.; Coronado, J.M.; Belver, C.; Lee, C.Y.; Augugliaro, V. Gas-phase photo-oxidation of toluene using nanometer-size TiO2 catalysts. *Appl. Catal. B Environ.* **2001**, *29*, 327–336. [CrossRef]

69. Augugliaro, V.; Coluccia, S.; Loddo, V.; Marchese, L.; Martra, G.; Palmisano, L.; Schiavello, M. Photocatalytic oxidation of gaseous toluene on anatase TiO2 catalyst: Mechanistic aspects and FT-IR investigation. *Appl. Catal. B Environ.* **1999**, *20*, 15–27. [CrossRef]

70. Zhang, L.; Menendez-Flores, V.M.; Murakami, N.; Ohno, T. Improvement of photocatalytic activity of brookite titanium dioxide nanorods by surface modification using chemical etching. *Appl. Surf. Sci.* **2012**, *258*, 5803–5809. [CrossRef]

71. Li, J.-J.; Yu, E.-Q.; Cai, S.-C.; Chen, X.; Chen, J.; Jia, H.-P.; Xu, Y.-J. Noble metal free, CeO$_2$/LaMnO$_3$ hybrid achieving efficient photo-thermal catalytic decomposition of volatile organic compounds under IR light. *Appl. Catal. B Environ.* **2019**, *240*, 141–152. [CrossRef]

72. Kong, J.; Xiang, Z.; Li, G.; An, T. Introduce oxygen vacancies into CeO$_2$ catalyst for enhanced coke resistance during photothermocatalytic oxidation of typical VOCs. *Appl. Catal. B Environ.* **2020**, *269*, 118755. [CrossRef]

73. Shayegan, Z.; Lee, C.-S.; Haghighat, F. TiO2 photocatalyst for removal of volatile organic compounds in gas phase—A review. *Chem. Eng. J.* **2018**, *334*, 2408–2439. [CrossRef]

74. Huang, Y.; Ho, S.; Lu, Y.; Niu, R.; Xu, L.; Cao, J.; Lee, S. Removal of Indoor Volatile Organic Compounds via Photocatalytic Oxidation: A Short Review and Prospect. *Molecules* **2016**, *21*, 56. [CrossRef] [PubMed]

75. Koli, V.B.; Kim, J.-S. Photocatalytic oxidation for removal of gases toluene by TiO2-CeO2 nanocomposites under UV light irradiation. *Mater. Sci. Semicond. Process.* **2019**, *94*, 70–79. [CrossRef]

76. Muñoz-Batista, M.J.; Gómez-Cerezo, M.N.; Kubacka, A.; Tudela, D.; Fernández-García, M. Role of interface contact in CeO2-TiO2 photocatalytic composite materials. *ACS Catal.* **2014**, *4*, 63–72. [CrossRef]

77. Yamakata, A.; Vequizo, J.J.M. Curious behaviors of photogenerated electrons and holes at the defects on anatase, rutile, and brookite TiO2 powders: A review. *J. Photochem. Photobiol. C Photochem. Rev.* **2019**, *40*, 234–243. [CrossRef]

78. Scirè, S.; Riccobene, P.M.; Crisafulli, C. Ceria supported group IB metal catalysts for the combustion of volatile organic compounds and the preferential oxidation of CO. *Appl. Catal. B Environ.* **2010**, *101*, 109–117. [CrossRef]

79. Scirè, S.; Fiorenza, R.; Gulino, A.; Cristaldi, A.; Riccobene, P.M. Selective oxidation of CO in H2-rich stream over ZSM5 zeolites supported Ru catalysts: An investigation on the role of the support and the Ru particle size. *Appl. Catal. A Gen.* **2016**, *520*, 82–91. [CrossRef]

80. Fiorenza, R.; Spitaleri, L.; Gulino, A.; Scirè, S. Ru–Pd bimetallic catalysts supported on CeO2-MnOx oxides as efficient systems for H2 purification through CO preferential Oxidation. *Catalysts* **2018**, *8*, 203. [CrossRef]

81. Gulino, A. Structural and electronic characterization of self-assembled molecular nanoarchitectures by X-ray photoelectron spectroscopy. *Anal. Bioanal. Chem.* **2013**, *405*, 1479–1495. [CrossRef]

82. Cantarella, M.; Di Mauro, A.; Gulino, A.; Spitaleri, L.; Nicotra, G.; Privitera, V.; Impellizzeri, G. Selective photodegradation of paracetamol by molecularly imprinted ZnO nanonuts. *Appl. Catal. B Environ.* **2018**, *238*, 509–517. [CrossRef]